



# Positivity preserving finite difference methods for Poisson–Nernst–Planck equations with steric interactions: Application to slit-shaped nanopore conductance



Jie Ding<sup>a</sup>, Zhongming Wang<sup>b</sup>, Shenggao Zhou<sup>a,\*</sup>

<sup>a</sup> Department of Mathematics and Mathematical Center for Interdiscipline Research, Soochow University, 1 Shizi Street, Suzhou 215006, Jiangsu, China

<sup>b</sup> Department of Mathematics and Statistics, Florida International University, Miami, FL, 33199, USA

## ARTICLE INFO

### Article history:

Received 14 September 2018

Received in revised form 27 June 2019

Accepted 31 July 2019

Available online 5 August 2019

### Keywords:

Poisson–Nernst–Planck equations

Steric interactions

Positivity

Condition number

Nanopore conductance

## ABSTRACT

To study ion transport in electrolyte solutions, we propose numerical methods for a modified Poisson–Nernst–Planck model with ionic steric effects (SPNP). Positivity preserving schemes based on harmonic-mean approximations are proposed on a non-uniform mesh for the spatial discretization of the SPNP equations. Both explicit and semi-implicit discretization are considered in time. Numerical analysis shows that explicit forward Euler and semi-implicit trapezoidal discretization lead to schemes that maintain fully discrete solution positivity under a constraint on a mesh ratio, while the semi-implicit backward Euler discretization maintain fully discrete solution positivity *unconditionally*. We further study the condition numbers of the matrix associated with the semi-implicit backward Euler discretization, and establish an upper bound on condition numbers, indicating that the developed discretization based on harmonic-mean approximations effectively solves the issue of the presence of large condition numbers when using the Slotboom-type variables. Further numerical simulations confirm the analysis results on accuracy, positivity, and bounded condition numbers. The proposed schemes are also applied to study practical applications, such as the impact of self and cross steric interactions on ion distribution and rectifying behavior in a slit-shaped nanopore with surface charges. Possible extensions of the numerical methods to other modified PNP models with ion correlations and steric effects are also discussed.

© 2019 Elsevier Inc. All rights reserved.

## 1. Introduction

The classical Poisson–Nernst–Planck (PNP) equations have been widely used to describe charge transport in applications including semiconductors [34], ion channels [49], and electrochemical energy devices [2]. Despite its many successes in various applications, the PNP model predicts unphysical crowding of ions near charged surfaces and incorrect dynamics of ion transport, due to the neglected steric effects of ions in its mean-field derivation. Recent years have seen a growing interest in incorporating steric effects under the framework of the PNP model. Several versions of the modified PNP theory have been developed in the literature to account for steric effects [17–19,21,23,33,35,40,43]. For instance, a size-modified

\* Corresponding author.

E-mail address: [sgzhou@suda.edu.cn](mailto:sgzhou@suda.edu.cn) (S. Zhou).

PNP theory has been proposed via the inclusion of the entropy of solvent molecules in the electrostatic free-energy functional [19,21,33]. Another strategy is to include the Lennard-Jones (LJ) interaction energy among ions in the free-energy functional [18,23]. To avoid computationally intractable integro-differential equations, local approximations of the nonlocal LJ integrals are employed to obtain local PNP models with steric effects [17,18].

In this work, we start with a free-energy functional that includes ionic steric interactions, and derive the Poisson–Nernst–Planck equations with steric interactions (SPNP):

$$\begin{cases} \partial_t c^l = \gamma^l \nabla \cdot \left( \nabla c^l + q^l c^l \nabla \psi + c^l \sum_{r=1}^M \omega_{lr} \nabla c^r \right), & l = 1, 2, \dots, M, \\ -\kappa \Delta \psi = \left( \sum_{l=1}^M q^l c^l + \rho^f \right). \end{cases} \quad (1.1)$$

Here  $\psi$  is the electrostatic potential,  $c^l$  is the ion concentration for the  $l$ th species,  $q^l$  is the corresponding valence,  $\rho^f$  is the fixed charge density,  $\kappa$  and  $\gamma^l$  are coefficients arising from nondimensionalization, and  $\omega_{lr}$  is the second-order virial coefficients depending on the size of  $l$ th and  $r$ th species of ions.

The classical PNP equations (with virial coefficient matrix  $W = (\omega_{lr}) = 0$ ) can hardly be solved analytically due to the nonlinear coupling of the electrostatic potential and ion concentrations. Theoretical results on the global existence, uniqueness, and asymptotic behavior of the PNP equations have been extensively studied in the literature of semiconductors [7, 8, 11, 38]. For the SPNP equations (1.1), the existence and uniqueness of the solutions have been established under the assumption that the virial coefficient matrix  $W$  is positive definite. Of interest is that the SPNP equations may admit multiple steady-state solutions when the matrix  $W$  is indefinite [14, 24]. Such multiple steady-state solutions correspond to different conductance states of ion channels, relating to the opening and closing states [5, 15].

Compared with limited theoretical results, much effort has been devoted to the development of numerical methods in various applications for the classical PNP equations [4, 6, 9, 10, 13, 25, 26, 32, 36, 37, 39, 43, 50]. Due to the physical faithfulness, it is desirable and crucial to preserve positivity of numerical solutions that represent ion concentrations. For instance, a finite difference scheme was proposed for the one-dimensional PNP equations, and it was proved to respect positivity under assumptions that the gradient of the electrostatic potential is bounded and time step size satisfies certain constraint conditions [10]. Inspired by the transformation (also known as the Slotboom variables) in [27, 28] for the Fokker–Planck equations, Liu and Wang [25] developed a finite difference scheme that is proved to ensure positivity under a constraint on the mesh ratio in the one-dimensional case. They also developed a discontinuous Galerkin method, in which the positivity of numerical solutions was enforced by an accuracy-preserving limiter [26]. A finite element method that can guarantee positivity of numerical solutions was developed for the PNP equations [36].

Many efforts have been devoted to the development of positivity-preserving numerical methods for the classical PNP equations. However, numerical methods with positivity-preserving properties are not well studied for the modified PNP theories with steric effects. In addition, the abovementioned positivity-preserving numerical methods are all designed for closed systems with zero-flux boundary conditions for ion concentrations. Open systems are often of practical interest, e.g., an ion channel system with two openings connected to bulk reservoirs. Our goal in this work is to develop positivity-preserving numerical methods for the PNP equations with steric effects, which are derived from an electrostatic free-energy functional that incorporates ionic steric interaction energy. The modified Nernst–Planck (NP) equations with steric interactions are reformulated with the generalized Slotboom variables for the purpose of designing proper numerical methods. Central differencing schemes based on harmonic-mean approximations are proposed on a nonuniform mesh for the spatial discretization of the reformulated NP equations. Our numerical analysis demonstrates that a temporal semi-implicit discretization leads to a full discrete scheme that guarantees positivity *unconditionally*, while an explicit or trapezoidal discretization gives rise to one that maintains positivity under a constraint on a mesh ratio.

Large condition numbers are often accompanied with the spatial discretization based on the Slotboom variables. Detailed numerical analysis on the semi-implicit discretization matrix establishes an estimate on the upper bound of the condition numbers. Further numerical tests confirm the analysis results on numerical accuracy, positivity, and bounded condition numbers. The proposed schemes are also applied to probe the impact of self and cross steric interactions on ion distribution and rectifying behavior of a slit-shaped nanopore with surface charges. It is of significance to note that the developed numerical approaches can be employed to design positivity-preserving numerical schemes for other modified PNP theories with ion correlations and steric effects.

The rest of this paper is organized as follows. In Section 2, we derive the SPNP equations with steric interactions from a free-energy functional. In Section 3, we give some details of our settings, and present finite difference methods along with desired discrete properties, including positivity and estimate on the upper bound of condition numbers of the matrix associated with a semi-implicit scheme. Section 4 presents some numerical tests on accuracy, steric effects, and rectification, etc. Finally, we conclude and discuss further improvements in Section 5.

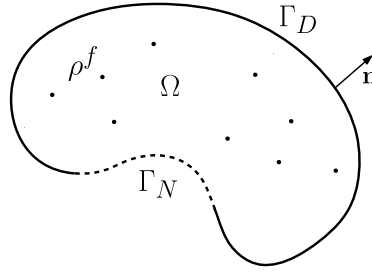


**Fig. 2.1.** Schematic illustration of a charged system occupying a domain  $\Omega$ . The boundary  $\partial\Omega = \Gamma_D \cup \Gamma_N$  with  $\Gamma_D \cap \Gamma_N = \emptyset$ , where the Dirichlet-type boundary  $\Gamma_D$  is shown in a solid curve and the Neumann-type boundary  $\Gamma_N$  is shown in a dotted curve. The distribution of fixed charges is given by  $\rho^f$ , and the normal vector to the boundary is denoted by  $\mathbf{n}$ .

## 2. Free energy and governing equations

### 2.1. Free energy

We consider a charged system that includes fixed charges  $\rho^f$  and mobile ions of  $M$  species occupying a bounded, open, connected domain  $\Omega$  with a smooth boundary  $\partial\Omega$ ; cf. Fig. 2.1. The boundary  $\partial\Omega$  may include two disjoint and smooth parts: Dirichlet-type boundary  $\Gamma_D$  and Neumann-type boundary  $\Gamma_N$ , where  $\Gamma_D \cap \Gamma_N = \emptyset$  and  $\Gamma_D \cup \Gamma_N = \partial\Omega$ . This setting covers the cases that  $\Gamma_D = \emptyset$  and  $\Gamma_N = \partial\Omega$  and that  $\Gamma_N = \emptyset$  and  $\Gamma_D = \partial\Omega$ . We assume that the electrostatic potential on  $\Gamma_D$  is given by  $\psi_D$ , and a surface charge density on  $\Gamma_N$  is given by  $\sigma$ . Both the boundary data  $\psi_D : \Gamma_D \rightarrow \mathbb{R}$  and  $\sigma : \Gamma_N \rightarrow \mathbb{R}$  are given bounded and smooth functions. For each  $l$  ( $1 \leq l \leq M$ ), we denote by  $c^l = c^l(\mathbf{x})$  the local ion concentration of the  $l$ th ionic species at position  $\mathbf{x} \in \Omega$ . The electrostatic potential  $\psi$  satisfies the following boundary-value problem of the Poisson's equation:

$$\begin{cases} -\nabla \cdot \varepsilon_0 \varepsilon_r \nabla \psi = \rho & \text{in } \Omega, \\ \varepsilon_0 \varepsilon_r \frac{\partial \psi}{\partial \mathbf{n}} = \sigma & \text{on } \Gamma_N, \\ \psi = \psi_D & \text{on } \Gamma_D, \end{cases} \quad (2.1)$$

where  $\varepsilon_0$  is the vacuum permittivity,  $\varepsilon_r$  is the dielectric coefficient assumed to be bounded above and below by positive constants, and  $\rho$  is the charge density given by

$$\rho = \sum_{l=1}^M q^l c^l + \rho^f.$$

Here  $q^l = z^l e$  with  $e$  being the elementary charge and  $z^l$  being the valence of  $l$ th ionic species.

For convenience, we denote by  $c = (c_1, \dots, c_M)$ . We consider the free-energy functional of the charged system:

$$F[c] = F_{\text{pot}}[c] + F_{\text{ent}}[c] + F_{\text{ster}}[c], \quad (2.2)$$

where the potential energy, entropic contribution, and steric interaction energy are given by

$$F_{\text{pot}}[c] = \frac{1}{2} \int_{\Omega} \rho \psi dV + \frac{1}{2} \int_{\Gamma_N} \sigma \psi dS - \frac{1}{2} \int_{\Gamma_D} \varepsilon_0 \varepsilon_r \frac{\partial \psi}{\partial \mathbf{n}} \psi_D dS,$$

$$F_{\text{ent}}[c] = \beta^{-1} \int_{\Omega} \sum_{l=1}^M c^l \left[ \ln(\Lambda^3 c^l) - 1 \right] dV,$$

$$F_{\text{ster}}[c] = \frac{1}{2} \beta^{-1} \int_{\Omega} c W c^T dV,$$

respectively. We note that the boundary contributions in  $F_{\text{pot}}[c]$  have been proposed in the work [31] to get a free energy being consistent with the governing equations with various boundary conditions. Here  $\beta$  is the inverse thermal energy and  $\Lambda$  is the thermal de Broglie wavelength. The interaction coefficient matrix is given by

$$W = (\omega_{ij})_{M \times M}, \quad (2.3)$$

where  $\omega_{ij}$  are the second-order virial coefficients for hard spheres, depending on the size of  $i$ th and  $j$ th ionic species [51]. Note that  $W$  is a symmetric matrix, and diagonal entries of  $W$  represent the self steric interaction of ions of the same species and off-diagonal entries represent cross steric interactions between ions of different species.

## 2.2. PNP equations with steric interactions

We shall derive the PNP equations with steric interactions based on the free-energy functional (2.2). Taking the first variation of the free-energy functional with respect to ion concentrations, we obtain the chemical potential  $\mu^l$  of the  $l$ th species of ions [31]:

$$\mu^l = \frac{\delta F[c]}{\delta c^l} = q^l \psi + \beta^{-1} \left[ \ln(\Lambda^3 c^l) + \sum_{r=1}^M w_{lr} c^r \right]. \quad (2.4)$$

We consider ion transport with steric interactions. The average velocity  $v^l$  of the  $l$ th ion species is determined by the balance between the hydrodynamic drag and thermodynamic force:

$$v^l \zeta^l = -\nabla \mu^l,$$

where  $\zeta^l$  is the friction coefficient. By the Einstein relation, we obtain

$$v^l = -\beta D^l \nabla \mu^l,$$

where  $D^l$  is the diffusion constant of the  $l$ th ionic species. By the continuity equation, we have

$$\partial_t c^l = -\nabla \cdot (c^l v^l) = \beta \nabla \cdot (D^l c^l \nabla \mu^l). \quad (2.5)$$

This, with the chemical potential (2.4), leads to the Nernst–Planck (NP) equation with steric interactions

$$\frac{\partial c^l}{\partial t} = \nabla \cdot D^l \left( \nabla c^l + \beta q^l c^l \nabla \psi + c^l \sum_{r=1}^M \omega_{lr} \nabla c^r \right).$$

To get a nondimensional formulation, we introduce a macroscopic length scale  $L$ , a characteristic screening length  $\lambda_D = \sqrt{\frac{\epsilon_0 \epsilon_r}{2\beta e^2 c_0}}$ , a characteristic concentration  $c_0$ , and the following dimensionless variables [2,20]

$$\tilde{\mathbf{x}} = \frac{\mathbf{x}}{L}, \quad \tilde{D}^l = \frac{D^l}{D_0}, \quad \tilde{t} = \frac{t D_0}{L \lambda_D}, \quad \tilde{c}^l = \frac{c^l}{c_0}, \quad \tilde{\rho}^f = \frac{\rho^f}{e c_0}, \quad \tilde{\sigma} = \frac{\sigma}{L e c_0}, \quad \tilde{\omega}_{lr} = c_0 \omega_{lr}, \quad \phi = \beta e \psi.$$

With above rescaling, we obtain by dropping all the tildes the nondimensionalized Poisson–Nernst–Planck equations with steric interactions (SPNP)

$$\begin{cases} \partial_t c^l = \gamma^l \nabla \cdot \left( \nabla c^l + z^l c^l \nabla \phi + c^l \sum_{r=1}^M \omega_{lr} \nabla c^r \right), & l = 1, 2, \dots, M, \\ -\kappa \Delta \phi = \sum_{l=1}^M z^l c^l + \rho^f, \end{cases} \quad (2.6)$$

where  $\gamma^l = \frac{\lambda_D}{L} D^l$  and  $\kappa = 2 \frac{\lambda_D^2}{L^2}$ .

The SPNP equations (2.6) describes the electro-diffusion of ions with steric interactions, and its solution satisfies the following energy dissipation law.

**Theorem 2.1.** The solution to the SPNP equations (2.6) satisfies

$$\begin{aligned} \frac{d}{dt} F[c] &= - \sum_{l=1}^M \int_{\Omega} \frac{D^l}{\beta c^l} \left| \nabla c^l + \beta q^l c^l \nabla \psi + c^l \sum_{r=1}^M \omega_{lr} \nabla c^r \right|^2 dV \\ &\quad + \sum_{l=1}^M \int_{\partial\Omega} \beta D^l \mu^l c^l \frac{\partial \mu^l}{\partial \mathbf{n}} dS - \int_{\Gamma_D} \epsilon_0 \epsilon_r \frac{\partial \psi}{\partial \mathbf{n}} \partial_t \psi_D dS + \int_{\Gamma_N} \partial_t \sigma \psi dS. \end{aligned} \quad (2.7)$$

**Proof.** Taking a derivative with respect to time, we have

$$\begin{aligned} \frac{d}{dt} F[c] &= \int_{\Omega} \sum_{l=1}^M \mu^l \partial_t c^l dV + \frac{1}{2} \int_{\Omega} \rho \partial_t \psi - \psi \partial_t \rho dV + \frac{1}{2} \int_{\Gamma_N} \partial_t \sigma \psi + \sigma \partial_t \psi dS \\ &\quad - \frac{1}{2} \int_{\Gamma_D} \varepsilon_0 \varepsilon_r \left[ \partial_t \left( \frac{\partial \psi}{\partial \mathbf{n}} \right) \psi_D + \frac{\partial \psi}{\partial \mathbf{n}} \partial_t \psi_D \right] dS. \end{aligned} \quad (2.8)$$

By the Poisson's equation, we have

$$\frac{1}{2} \int_{\Omega} \rho \partial_t \psi - \psi \partial_t \rho dV = \frac{1}{2} \int_{\Gamma_N} \psi \partial_t \sigma - \sigma \partial_t \psi dS + \frac{1}{2} \int_{\Gamma_D} \varepsilon_0 \varepsilon_r \left[ \partial_t \left( \frac{\partial \psi}{\partial \mathbf{n}} \right) \psi_D - \frac{\partial \psi}{\partial \mathbf{n}} \partial_t \psi_D \right] dS.$$

It follows from (2.4) and (2.5) that

$$\frac{d}{dt} F[c] = \sum_{l=1}^M \int_{\partial \Omega} \beta D^l \mu^l c^l \frac{\partial \mu^l}{\partial \mathbf{n}} dS - \sum_{l=1}^M \int_{\Omega} \beta D^l c^l \left| \nabla \mu^l \right|^2 dV - \int_{\Gamma_D} \varepsilon_0 \varepsilon_r \frac{\partial \psi}{\partial \mathbf{n}} \partial_t \psi_D dS + \int_{\Gamma_N} \partial_t \sigma \psi dS.$$

Substituting (2.4) into the above equation completes the proof.  $\square$

In (2.7), we observe the standard free-energy dissipation in  $\Omega$ , as well as energy exchange through boundaries. When zero-flux boundary conditions are imposed and the boundary data,  $\sigma$  and  $\psi_D$ , are independent of time, we have the energy dissipation law  $\frac{dF}{dt} \leq 0$ .

**Remark 2.1.** The same model based on local approximations of Lennard-Jones interactions has been proposed in the works [14,15,17,18,23,24,43]. While both models include steric effects, the interaction coefficients  $W$  have different interpretations in two models.

### 3. Numerical methods and properties

We propose numerical methods for the initial-boundary value problem of the SPNP equations:

$$\begin{cases} \partial_t c^l = \gamma^l \nabla \cdot \left( \nabla c^l + z^l c^l \nabla \phi + c^l \sum_{r=1}^M w_{lr} \nabla c^r \right), & t > 0, \quad l = 1, 2, \dots, M, \\ -\kappa \Delta \phi = \sum_{l=1}^M z^l c^l + \rho^f, \\ c^l(0, \cdot) = c_{in}^l(\cdot), \\ \kappa \frac{\partial \phi}{\partial \mathbf{n}} = \sigma(t), \quad \frac{\partial c^l}{\partial \mathbf{n}} + z^l c^l \frac{\partial \phi}{\partial \mathbf{n}} + c^l \sum_{r=1}^M w_{lr} \frac{\partial c^r}{\partial \mathbf{n}} = 0 \text{ on } \Gamma_N, \\ \phi = \phi_D(t), \quad c^l = c_D^l(t) \text{ on } \Gamma_D, \end{cases} \quad (3.1)$$

where  $c_{in}^l$  is the initial distribution of  $l$ th ion concentration, and Dirichlet boundary conditions for concentrations are imposed on the boundary  $\Gamma_D$  and zero-flux boundary conditions are imposed on the boundary  $\Gamma_N$ . To be more general, we here consider time-dependent boundary data. Such a set-up of boundary conditions has wide applications, e.g., ion transport in nanopores.

#### 3.1. Numerical scheme

For simplicity, we present our scheme in a rectangular domain  $\Omega = (a, b) \times (c, d)$  with boundaries

$$\Gamma_D = \{(x, y) : x = a \text{ or } b, c \leq y \leq d\} \text{ and } \Gamma_N = \{(x, y) : y = c \text{ or } d, a \leq x \leq b\}.$$

We introduce grid points

$$a = x_{\frac{1}{2}} < x_{\frac{3}{2}} < \dots < x_{N_x + \frac{1}{2}} = b,$$

$$c = y_{\frac{1}{2}} < y_{\frac{3}{2}} < \dots < y_{N_y + \frac{1}{2}} = d,$$

where  $N_x$  and  $N_y$  are the number of grid points along each dimension. Define

$$x_i = \frac{x_{i-\frac{1}{2}} + x_{i+\frac{1}{2}}}{2} \quad \text{and} \quad y_j = \frac{y_{j-\frac{1}{2}} + y_{j+\frac{1}{2}}}{2} \quad \text{for } i = 1, \dots, N_x, j = 1, \dots, N_y.$$

We cover the domain with a nonuniform mesh

$$\{x_i, y_j\} \quad \text{for } i = 1, \dots, N_x, j = 1, \dots, N_y,$$

with grid spacing given by

$$h_i^x = x_{i+\frac{1}{2}} - x_{i-\frac{1}{2}}, \quad h_j^y = y_{j+\frac{1}{2}} - y_{j-\frac{1}{2}} \quad \text{for } i = 1, \dots, N_x, j = 1, \dots, N_y,$$

and

$$h_{i+\frac{1}{2}}^x = x_{i+1} - x_i, \quad h_{j+\frac{1}{2}}^y = y_{j+1} - y_j \quad \text{for } i = 1, \dots, N_x - 1, j = 1, \dots, N_y - 1.$$

The semi-discrete  $c_{i,j}^l$ ,  $g_{i,j}^l$ , and  $\phi_{i,j}$  are used to denote the numerical approximations of  $c^l(t, x_i, y_j)$ ,  $g^l(t, x_i, y_j)$ , and  $\phi(t, x_i, y_j)$ , respectively.

To facilitate the presentation, we introduce discrete operators

$$D_x^+ f_{i,j} = \frac{f_{i+1,j} - f_{i,j}}{h_{i+\frac{1}{2}}^x}, \quad D_x^2 f_{i,j} = \frac{D_x^+ f_{i,j} - D_x^+ f_{i-1,j}}{h_i^x}.$$

Analogously, discrete operators  $D_y^+$ , and  $D_y^2$  can be defined. Also, we introduce

$$h_m^x = \min(h_1^x, \dots, h_{N_x}^x), \quad h_M^x = \max(h_1^x, \dots, h_{N_x}^x), \\ h_m^y = \min(h_1^y, \dots, h_{N_y}^y), \quad h_M^y = \max(h_1^y, \dots, h_{N_y}^y).$$

### 1) Solving Poisson's equation

Given  $c_{i,j}^l$ , the Poisson's equation is approximated by a central differencing stencil

$$-\kappa(D_x^2 + D_y^2)\phi_{i,j} = \left( \sum_{l=1}^M z^l c_{i,j}^l + \rho_{i,j}^f \right), \quad i = 1, \dots, N_x, j = 1, \dots, N_y. \quad (3.2)$$

The Dirichlet boundary conditions on  $\Gamma_D$  are discretized by

$$\frac{\phi_{0,j} + \phi_{1,j}}{2} = \phi_D(t, a, y_j), \quad \frac{\phi_{N_x+1,j} + \phi_{N_x,j}}{2} = \phi_D(t, b, y_j) \quad \text{for } j = 1, \dots, N_y. \quad (3.3)$$

The Neumann boundary conditions on  $\Gamma_N$  are discretized by

$$-\kappa D_y^+ \phi_{i,0} = \sigma(t, x_i, c), \quad \kappa D_y^+ \phi_{i,N_y} = \sigma(t, x_i, d) \quad \text{for } i = 1, \dots, N_x. \quad (3.4)$$

For ease of presentation, we have extended the definition of the boundary data  $\phi_D$  and  $\sigma$  to the whole domain. We note that the ghost points outside  $\Omega$  are eliminated in numerical computations by coupling the discretization stencil (3.2) and boundary discretization (3.3) and (3.4).

### 2) Spatial discretization of NP equations

The discretization of the Nernst–Planck equation with steric interactions is based on a reformulation

$$\partial_t c^l = \gamma^l \nabla \cdot (e^{-S^l} \nabla g^l), \quad (3.5)$$

where  $S^l = q^l \phi + \sum_{r=1}^M w_{lr} c^r$  and  $g^l = c^l e^{S^l}$ , which is generalized Slotboom variables [26,32].

Spatial discretization of Eq. (3.5) at  $\{x_i, y_j\}$  leads to a semi-discrete scheme

$$h_i^x h_j^y \frac{d}{dt} c_{i,j}^l = \gamma^l h_j^y \left( e^{-S_{i+\frac{1}{2},j}^l} \widehat{g}_{x,i+\frac{1}{2},j}^l - e^{-S_{i-\frac{1}{2},j}^l} \widehat{g}_{x,i-\frac{1}{2},j}^l \right) \\ + \gamma^l h_i^x \left( e^{-S_{i,j+\frac{1}{2}}^l} \widehat{g}_{y,i,j+\frac{1}{2}}^l - e^{-S_{i,j-\frac{1}{2}}^l} \widehat{g}_{y,i,j-\frac{1}{2}}^l \right) := Q_{i,j}(c^l, S^l), \quad (3.6)$$

where central differencing is used for the flux

$$\hat{g}_{x,i+\frac{1}{2},j}^l = \frac{c_{i+1,j}^l e^{S_{i+1,j}^l} - c_{i,j}^l e^{S_{i,j}^l}}{h_{i+\frac{1}{2}}^x} \text{ and } \hat{g}_{y,i,j+\frac{1}{2}}^l = \frac{c_{i,j+1}^l e^{S_{i,j+1}^l} - c_{i,j}^l e^{S_{i,j}^l}}{h_{j+\frac{1}{2}}^y}, \quad (3.7)$$

and harmonic-mean approximations at half-grid points are used:

$$e^{-S_{i+\frac{1}{2},j}^l} = \frac{2e^{-S_{i+1,j}^l} e^{-S_{i,j}^l}}{e^{-S_{i+1,j}^l} + e^{-S_{i,j}^l}} \text{ and } e^{-S_{i,j+\frac{1}{2}}^l} = \frac{2e^{-S_{i,j+1}^l} e^{-S_{i,j}^l}}{e^{-S_{i,j+1}^l} + e^{-S_{i,j}^l}}. \quad (3.8)$$

We note that, instead of geometric-mean approximations that are often used in the Slotboom transformation, the main originality of our scheme is the use of harmonic-mean approximations, which give bounded coefficients in the discretization stencil.

The Dirichlet boundary conditions on  $\Gamma_D$  are discretized by

$$\begin{aligned} \frac{c_{0,j}^l + c_{1,j}^l}{2} &= c_D^l(t, a, y_j) := c_{D,\frac{1}{2},j}^l(t), \\ \frac{c_{N_x+1,j}^l + c_{N_x,j}^l}{2} &= c_D^l(t, b, y_j) := c_{D,N_x+\frac{1}{2},j}^l(t), \quad j = 1, \dots, N_y. \end{aligned} \quad (3.9)$$

The zero-flux boundary conditions on  $\Gamma_N$  are discretized by

$$\hat{g}_{y,i,\frac{1}{2}}^l = 0, \quad \hat{g}_{y,i,N_y+\frac{1}{2}}^l = 0, \quad i = 1, \dots, N_x. \quad (3.10)$$

### 3) Time discretization of NP equations

With a uniform time step size  $\Delta t$  and  $t_n = n\Delta t$ ,  $c_{i,j}^{l,n}$ ,  $g_{i,j}^{l,n}$ , and  $S_{i,j}^{l,n}$  are used to denote the numerical approximations of  $c^l(t_n, x_i, y_j)$ ,  $g^l(t_n, x_i, y_j)$ , and  $S^l(t_n, x_i, y_j)$ , respectively.

We propose three time discretizations:

#### 1) First-order explicit forward Euler scheme

$$h_i^x h_j^y \frac{c_{i,j}^{l,n+1} - c_{i,j}^{l,n}}{\Delta t} = Q_{i,j}(c^{l,n}, S^{l,n}), \quad (3.11)$$

#### 2) First-order semi-implicit backward Euler scheme

$$h_i^x h_j^y \frac{c_{i,j}^{l,n+1} - c_{i,j}^{l,n}}{\Delta t} = Q_{i,j}(c^{l,n+1}, S^{l,n}), \quad (3.12)$$

#### 3) Second-order semi-implicit trapezoidal scheme

$$h_i^x h_j^y \frac{c_{i,j}^{l,n+1} - c_{i,j}^{l,n}}{\Delta t} = Q_{i,j}\left(\frac{c^{l,n} + c^{l,n+1}}{2}, S^{l,n}\right), \quad (3.13)$$

where the boundary data are evaluated at  $t_n$ ,  $t_{n+1}$ , and  $t_{n+1/2}$ , respectively.

## 3.2. Numerical properties

One of the main advantages of the proposed finite difference schemes is that all schemes (3.11)–(3.13) maintain the positivity of numerical solutions at discrete level.

### Theorem 3.1.

(1) The numerical solutions  $c_{i,j}^{l,n+1}$  computed from the forward Euler scheme (3.11) remain positive in time, i.e., if  $c_{i,j}^{l,n} > 0$ , then

$$c_{i,j}^{l,n+1} > 0 \text{ for } i = 1, \dots, N_x, \quad j = 1, \dots, N_y,$$

if the mesh ratio satisfies

$$\Delta t \leq \frac{(h_m^x)^2 (h_m^y)^2}{4 \max_{1 \leq l \leq M} \gamma^l [h_m^x h_M^x + h_m^y h_M^y]}.$$

- (2) The numerical solutions  $c_{i,j}^{l,n+1}$  computed from the backward Euler scheme (3.12) remain positive in time unconditionally.  
(3) The numerical solutions  $c_{i,j}^{l,n+1}$  computed from the trapezoidal scheme (3.13) remain positive in time if

$$\Delta t \leq \frac{(h_m^x)^2 (h_m^y)^2}{2 \max_{1 \leq l \leq M} \gamma^l [h_m^x h_M^x + h_m^y h_M^y]}.$$

**Proof.** (1) Define discrete operators

$$\mathcal{H}_x^\pm S_{i,j}^{l,n} := \frac{e^{-S_{i\pm 1,j}^{l,n}}}{e^{-S_{i,j}^{l,n}} + e^{-S_{i\pm 1,j}^{l,n}}} \text{ and } \mathcal{H}_y^\pm S_{i,j}^{l,n} := \frac{e^{-S_{i,j\pm 1}^{l,n}}}{e^{-S_{i,j}^{l,n}} + e^{-S_{i,j\pm 1}^{l,n}}}.$$

Without any assumption on  $S_{i,j}^{l,n}$ , the following crucial inequality holds unconditionally:

$$0 < \mathcal{H}_k^\pm S_{i,j}^{l,n} \leq 1 \text{ for } k = x, y. \quad (3.14)$$

The explicit scheme (3.11) can be rewritten as

$$\begin{aligned} h_i^x h_j^y c_{i,j}^{l,n+1} = & h_i^x h_j^y c_{i,j}^{l,n} - 2\gamma^l \Delta t c_{i,j}^{l,n} \left( \frac{h_j^y}{h_{i+\frac{1}{2}}^x} \mathcal{H}_x^+ + \frac{h_j^y}{h_{i-\frac{1}{2}}^x} \mathcal{H}_x^- + \frac{h_i^x}{h_{j+\frac{1}{2}}^y} \mathcal{H}_y^+ + \frac{h_i^x}{h_{j-\frac{1}{2}}^y} \mathcal{H}_y^- \right) S_{i,j}^{l,n} \\ & + 2\gamma^l \Delta t \left( \frac{h_j^y}{h_{i+\frac{1}{2}}^x} c_{i+1,j}^{l,n} \mathcal{H}_x^- S_{i+1,j}^{l,n} + \frac{h_j^y}{h_{i-\frac{1}{2}}^x} c_{i-1,j}^{l,n} \mathcal{H}_x^+ S_{i-1,j}^{l,n} \right) \\ & + 2\gamma^l \Delta t \left( \frac{h_i^x}{h_{j+\frac{1}{2}}^y} c_{i,j+1}^{l,n} \mathcal{H}_y^- S_{i,j+1}^{l,n} + \frac{h_i^x}{h_{j-\frac{1}{2}}^y} c_{i,j-1}^{l,n} \mathcal{H}_y^+ S_{i,j-1}^{l,n} \right). \end{aligned}$$

It follows from the inequalities (3.14) that the numerical solution  $c_{i,j}^{l,n+1}$  is positive if  $c_{i,j}^{l,n} > 0$ , when

$$\Delta t \leq \frac{(h_m^x)^2 (h_m^y)^2}{4\gamma^l [h_m^x h_M^x + h_m^y h_M^y]} \quad \text{for } l = 1, \dots, M.$$

This completes the proof.

(2) We consider the semi-implicit discretization scheme (3.12) at interior, edge, and vertices grid points. Along with the discretization of boundary conditions, the full discretization scheme (3.12) can be expressed in a matrix form

$$L(c^{l,n+1} - c^{l,n}) = A^l c^{l,n+1} + \xi^l,$$

where the diagonal matrix

$$L = \text{diag} \left( h_1^x h_1^y, \dots, h_1^x h_{N_y}^y, h_2^x h_1^y, \dots, h_2^x h_{N_y}^y, \dots, h_{N_x}^x h_1^y, \dots, h_{N_x}^x h_{N_y}^y \right),$$

$A^l$  is a coefficient matrix resulting from discretization, and  $c^{l,n}$  and  $c^{l,n+1}$  are column vectors with components  $c_{i,j}^{l,n}$  and  $c_{i,j}^{l,n+1}$ , respectively. Here the column vector  $\xi^l$  resulting from the Dirichlet boundary data is given by

$$\begin{aligned} \xi^l = 4\gamma^l \Delta t & \left( \underbrace{\frac{h_1^y}{h_{\frac{1}{2}}^x} c_{D,\frac{1}{2},1}^{l,n+1} \mathcal{H}_x^+ S_{0,1}^{l,n}, \dots, \frac{h_{N_y}^y}{h_{\frac{1}{2}}^x} c_{D,\frac{1}{2},N_y}^{l,n+1} \mathcal{H}_x^+ S_{0,N_y}^{l,n}, \underbrace{0, \dots, 0}_{N_y(N_x-2)}}_{N_y} \right. \\ & \left. \underbrace{\frac{h_1^y}{h_{N_x+\frac{1}{2}}^x} c_{D,N_x+\frac{1}{2},1}^{l,n+1} \mathcal{H}_x^- S_{N_x+1,1}^{l,n}, \dots, \frac{h_{N_y}^y}{h_{N_x+\frac{1}{2}}^x} c_{D,N_x+\frac{1}{2},N_y}^{l,n+1} \mathcal{H}_x^- S_{N_x+1,N_y}^{l,n}}_{N_y} \right)^T. \end{aligned}$$

Clearly,  $\xi_k^l \geq 0$  for  $k = 1, \dots, N_x N_y$ . We now go through the nonzero entries in each column of the matrix  $A^l$ . Define

$$[i, j] := (i - 1)N_y + j \quad \text{for } i = 1, \dots, N_x, \quad j = 1, \dots, N_y.$$

We shall show that

$$\begin{cases} \sum_{m=1}^{N_x N_y} A_{m,n}^l \leq 0 & \text{for } n = 1, \dots, N_x N_y, \\ A_{n,n}^l < 0 & \text{for } n = 1, \dots, N_x N_y, \\ A_{m,n}^l > 0 & \text{for } n, m = 1, \dots, N_x N_y, \text{ and } m \neq n. \end{cases} \quad (3.15)$$

We examine the  $k$ th column of the matrix  $A^l$ , with  $k = [i, j]$ . The column is composed of coefficients of the stencils that involve the unknown  $c_{i,j}^{l,n+1}$  associated to the grid point  $\{x_i, y_j\}$ . To prove (3.15), we look into all of the discretization stencils involving different types of grid points.

First, for any interior grid point  $\{x_i, y_j\}$  with  $i = 2, \dots, N_x - 1$  and  $j = 2, \dots, N_y - 1$ , non-zero entries of the  $k$ th column ( $k = [i, j]$ ) are given by

$$A_{m,k}^l = \begin{cases} 2\gamma^l \Delta t \frac{h_j^y}{h_{i-\frac{1}{2}}^x} \mathcal{H}_x^- S_{i,j}^{l,n}, & m = [i-1, j], \\ 2\gamma^l \Delta t \frac{h_i^x}{h_{j-\frac{1}{2}}^y} \mathcal{H}_y^- S_{i,j}^{l,n}, & m = [i, j-1], \\ -2\gamma^l \Delta t \left( \frac{h_j^y}{h_{i+\frac{1}{2}}^x} \mathcal{H}_x^+ S_{i,j}^{l,n} + \frac{h_j^y}{h_{i-\frac{1}{2}}^x} \mathcal{H}_x^- S_{i,j}^{l,n} \right. \\ \left. + \frac{h_i^x}{h_{j+\frac{1}{2}}^y} \mathcal{H}_y^+ S_{i,j}^{l,n} + \frac{h_i^x}{h_{j-\frac{1}{2}}^y} \mathcal{H}_y^- S_{i,j}^{l,n} \right), & m = k, \\ 2\gamma^l \Delta t \frac{h_i^x}{h_{j+\frac{1}{2}}^y} \mathcal{H}_y^+ S_{i,j}^{l,n}, & m = [i, j+1], \\ 2\gamma^l \Delta t \frac{h_j^y}{h_{i+\frac{1}{2}}^x} \mathcal{H}_x^+ S_{i,j}^{l,n}, & m = [i+1, j]. \end{cases}$$

Hence, the conclusion (3.15) holds for the columns associated to interior grid points. We examine the conclusion for boundary grid points that are adjacent to four edges but not vertices. We consider Dirichlet boundary grid points  $\{x_1, y_j\}$  for  $j = 2, \dots, N_y - 1$ , and Neumann boundary grid points  $\{x_i, y_1\}$  for  $i = 2, \dots, N_x - 1$ . Non-zero entries of the  $k$ th column ( $k = [1, j]$ ) are

$$A_{m,k}^l = \begin{cases} 2\gamma^l \Delta t \frac{h_1^x}{h_{j-\frac{1}{2}}^y} \mathcal{H}_y^- S_{1,j}^{l,n}, & m = [1, j-1], \\ -2\gamma^l \Delta t \left( \frac{h_j^y}{h_{\frac{1}{2}}^x} + \frac{h_j^y}{h_{\frac{3}{2}}^x} \mathcal{H}_x^+ S_{1,j}^{l,n} + \frac{h_1^x}{h_{j+\frac{1}{2}}^y} \mathcal{H}_y^+ S_{1,j}^{l,n} + \frac{h_1^x}{h_{j-\frac{1}{2}}^y} \mathcal{H}_y^- S_{1,j}^{l,n} \right), & m = k, \\ 2\gamma^l \Delta t \frac{h_1^x}{h_{j+\frac{1}{2}}^y} \mathcal{H}_y^+ S_{1,j}^{l,n}, & m = [1, j+1], \\ 2\gamma^l \Delta t \frac{h_j^y}{h_{\frac{3}{2}}^x} \mathcal{H}_x^+ S_{1,j}^{l,n}, & m = [2, j]. \end{cases}$$

Non-zero entries of the  $k$ th column ( $k = [i, 1]$ ) are

$$A_{m,k}^l = \begin{cases} 2\gamma^l \Delta t \frac{h_1^y}{h_{i-\frac{1}{2}}^x} \mathcal{H}_x^- S_{1,j}^{l,n}, & m = [i-1, 1], \\ -2\gamma^l \Delta t \left( \frac{h_1^y}{h_{i+\frac{1}{2}}^x} \mathcal{H}_x^+ S_{1,j}^{l,n} + \frac{h_1^y}{h_{i-\frac{1}{2}}^x} \mathcal{H}_x^- S_{1,j}^{l,n} + \frac{h_i^x}{h_{\frac{3}{2}}^y} \mathcal{H}_y^+ S_{1,j}^{l,n} \right), & m = k, \\ 2\gamma^l \Delta t \frac{h_i^x}{h_{\frac{3}{2}}^y} \mathcal{H}_y^+ S_{1,j}^{l,n}, & m = [i, 2], \\ 2\gamma^l \Delta t \frac{h_1^y}{h_{i+\frac{1}{2}}^x} \mathcal{H}_x^+ S_{1,j}^{l,n}, & m = [i+1, 1]. \end{cases}$$

Thus, the conclusion (3.15) holds for the columns associated to edge grid points. For vertices grid points, e.g.,  $k = [1, 1]$ , we have

$$A_{m,k}^l = \begin{cases} -2\gamma^l \Delta t \left( \frac{h_1^y}{h_{\frac{1}{2}}^x} + \frac{h_1^y}{h_{\frac{3}{2}}^x} \mathcal{H}_x^+ S_{1,1}^{l,n} + \frac{h_1^x}{h_{\frac{3}{2}}^y} \mathcal{H}_y^+ S_{1,1}^{l,n} \right), & m = k, \\ 2\gamma^l \Delta t \frac{h_1^x}{h_{\frac{3}{2}}^y} \mathcal{H}_y^+ S_{1,1}^{l,n}, & m = [1, 2], \\ 2\gamma^l \Delta t \frac{h_1^y}{h_{\frac{3}{2}}^x} \mathcal{H}_x^+ S_{1,1}^{l,n}, & m = [2, 1]. \end{cases}$$

Again, the conclusion (3.15) holds for the columns corresponding to vertices grid points.

In summary, the conclusion (3.15) holds true for each column of the coefficient matrix  $A^l$ . With (3.14), we further have

$$\begin{cases} \sum_{m=1}^{N_x N_y} A_{m,n}^l = 0 \text{ for } n = [i, j] \text{ with } i = 2, \dots, N_x - 1 \text{ and } j = 2, \dots, N_y - 1, \\ \sum_{m=1}^{N_x N_y} A_{m,n}^l = -2\gamma^l \Delta t \frac{h_j^y}{h_{\frac{1}{2}}^x} \text{ for } n = [1, j] \text{ with } 1 \leq j \leq N_y, \\ \sum_{m=1}^{N_x N_y} A_{m,n}^l = -2\gamma^l \Delta t \frac{h_j^y}{h_{N+\frac{1}{2}}^x} \text{ for } n = [N_x, j] \text{ with } 1 \leq j \leq N_y, \\ -4\gamma^l \Delta t \left( \frac{h_M^y}{h_m^x} + \frac{h_M^x}{h_m^y} \right) \leq A_{m,m}^l < 0 \text{ for } m = 1, \dots, N_x N_y, \\ 0 < A_{m,n}^l \leq 2\gamma^l \Delta t \min \left\{ \frac{h_M^y}{h_m^x}, \frac{h_M^x}{h_m^y} \right\} \text{ for } m, n = 1, \dots, N_x N_y \text{ and } m \neq n. \end{cases} \quad (3.16)$$

The semi-implicit scheme can be expressed in a matrix form

$$B^l c^{l,n+1} = L c^{l,n} + \xi^l, \quad (3.17)$$

where  $B^l = L - A^l$ . According to the Gershgorin circle theorem, we have

$$\begin{aligned} \lambda_{B^l} &\in \left\{ z : \left| z - \left[ \frac{(h_M^x h_M^y + h_m^x h_m^y)}{2} + 4\gamma^l \Delta t \left( \frac{h_M^y}{h_m^x} + \frac{h_M^x}{h_m^y} \right) \right] \right| \right. \\ &\quad \left. \leq \frac{(h_M^x h_M^y - h_m^x h_m^y)}{2} + 4\gamma^l \Delta t \left( \frac{h_M^y}{h_m^x} + \frac{h_M^x}{h_m^y} \right) \right\}, \end{aligned} \quad (3.18)$$

where  $\lambda_{B^l}$  is an eigenvalue of  $B^l$  and  $|\cdot|$  represents the modulus. Let  $\eta$  be a number such that

$$\eta > \max_{1 \leq l \leq M} \left[ h_M^x h_M^y + 8\gamma^l \Delta t \left( \frac{h_M^y}{h_m^x} + \frac{h_M^x}{h_m^y} \right) \right].$$

Define  $P^l = \eta I - B^l$ , where  $I$  is an identity matrix. It follows from the entries of  $B^l$  that  $P^l$  is a non-negative matrix. Denote the eigenvalue of  $P^l$  by  $\lambda_{P^l}$ . From (3.18), we have

$$\begin{aligned} \lambda_{P^l} &\in \left\{ z : \left| z - \left[ \eta - \frac{(h_M^x h_M^y + h_m^x h_m^y)}{2} - 4\gamma^l \Delta t \left( \frac{h_M^y}{h_m^x} + \frac{h_M^x}{h_m^y} \right) \right] \right| \right. \\ &\quad \left. \leq \frac{(h_M^x h_M^y - h_m^x h_m^y)}{2} + 4\gamma^l \Delta t \left( \frac{h_M^y}{h_m^x} + \frac{h_M^x}{h_m^y} \right) \right\}, \end{aligned} \quad (3.19)$$

which indicates that  $\eta$  is greater than the maximum of the moduli of the eigenvalues of  $P^l$ . Therefore,  $B^l$  is an M-matrix and  $(B^l)^{-1}$  is non-negative. Since each component of the vector  $\xi^l$  is nonnegative, we have  $c_{i,j}^{l,n+1} > 0$ , given  $c_{i,j}^{l,n} > 0$ .

(3) The trapezoidal scheme (3.13) can be written as

$$\left( L - \frac{A^l}{2} \right) c^{l,n+1} = \left( L + \frac{A^l}{2} \right) c^{l,n} + \xi^l,$$

where  $A^l$  is the same as the matrix mentioned above. Similar to the proof in (2), we can show that  $\left( L - \frac{A^l}{2} \right)$  is an M-matrix unconditionally. Following the proof in (1), we know that  $\left( L + \frac{A^l}{2} \right)$  is a positive matrix if

$$\Delta t \leq \frac{(h_m^x)^2 (h_m^y)^2}{2 \max_{1 \leq l \leq M} \gamma^l [h_m^x h_M^x + h_m^y h_M^y]}.$$

With this condition, we have  $c_{i,j}^{l,n+1} > 0$ , given  $c_{i,j}^{l,n} > 0$ .  $\square$

**Theorem 3.2.** For the first-order semi-implicit scheme (3.12), the condition number of the coefficient matrix  $B^l$  in (3.17) satisfies

$$\kappa_1(B^l) := \|B^l\|_1 \|(B^l)^{-1}\|_1 \leq \frac{h_M^x h_M^y}{h_m^x h_m^y} + 8\gamma^l \Delta t \left[ \frac{h_M^y}{(h_m^x)^2 h_m^y} + \frac{h_M^x}{h_m^x (h_m^y)^2} \right] \quad (3.20)$$

and

$$\begin{aligned} \kappa_2(B^l) &:= \|B^l\|_2 \|(B^l)^{-1}\|_2 \\ &\leq \sqrt{N_x N_y} \left\{ \frac{h_M^x h_M^y}{h_m^x h_m^y} + 8\gamma^l \Delta t \left[ \frac{h_M^y}{(h_m^x)^2 h_m^y} + \frac{h_M^x}{h_m^x (h_m^y)^2} \right] \right\}. \end{aligned} \quad (3.21)$$

**Proof.** From (3.16), we have

$$\nu B^l = \theta,$$

where

$$\nu = (\underbrace{1, \dots, 1}_{N_x N_y})$$

and

$$\begin{aligned} \theta &= \left( h_1^x h_1^y + \gamma^l \Delta t \frac{h_1^y}{h_{\frac{1}{2}}^x}, \dots, h_1^x h_{N_y}^y + \gamma^l \Delta t \frac{h_{N_y}^y}{h_{\frac{1}{2}}^x}, \dots, h_i^x h_1^y, \dots, h_i^x h_{N_y}^y, \dots, \right. \\ &\quad \left. h_{N_x}^x h_1^y + \gamma^l \Delta t \frac{h_1^y}{h_{N_x + \frac{1}{2}}^x}, \dots, h_{N_x}^x h_{N_y}^y + \gamma^l \Delta t \frac{h_{N_y}^y}{h_{N_x + \frac{1}{2}}^x} \right). \end{aligned}$$

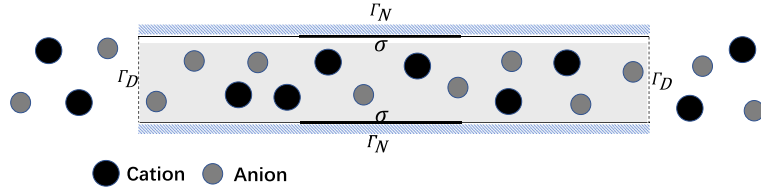


**Fig. 4.1.** A schematic view of a slit-shaped nanopore region  $\Omega = [0, 30] \times [0, 1]$  (in nanometer). The left and right boundaries are denoted by  $\Gamma_D$ , and the top and bottom boundaries are denoted by  $\Gamma_N$ . Surface charges are distributed on part of  $\Gamma_N$  indicated by bold lines.

Furthermore, we have  $\theta \geq h_m^x h_m^y v$ , in componentwise sense.

From the proof of Theorem 3.1, we know that  $B^l$  is an M-matrix, and therefore  $(B^l)^{-1}$  exists and is a non-negative matrix. We then have

$$h_m^x h_m^y v (B^l)^{-1} \leq v,$$

which implies that each column sum of  $(B^l)^{-1}$  is less or equal to  $\frac{1}{h_m^x h_m^y}$ . Since each entry of  $(B^l)^{-1}$  is non-negative, we have  $\|(B^l)^{-1}\|_1 \leq \frac{1}{h_m^x h_m^y}$ . Furthermore, it follows from (3.16) that

$$\|B^l\|_1 \leq h_M^x h_M^y + 8\gamma^l \Delta t \left( \frac{h_M^y}{h_m^x} + \frac{h_M^x}{h_m^y} \right).$$

By the definition of 1-norm condition number, we complete the proof of (3.20).

From non-zero entries of  $B^l$ , we have

$$\|B^l\|_\infty \leq h_M^x h_M^y + 8\gamma^l \Delta t \left( \frac{h_M^y}{h_m^x} + \frac{h_M^x}{h_m^y} \right).$$

By the results that [16]

$$\|B^l\|_2 \leq \sqrt{\|B^l\|_1 \|B^l\|_\infty} \text{ and } \|(B^l)^{-1}\|_2 \leq \sqrt{N_x N_y} \|(B^l)^{-1}\|_1,$$

we obtain

$$\kappa_2(B^l) \leq \sqrt{N_x N_y} \left\{ \frac{h_M^x h_M^y}{h_m^x h_m^y} + 8\gamma^l \Delta t \left[ \frac{h_M^y}{(h_m^x)^2 h_m^y} + \frac{h_M^x}{h_m^x (h_m^y)^2} \right] \right\}. \quad \square$$

**Remark 3.1.** Numerical studies in Section 4.1 show that the 2-norm condition number of  $B^l$  behaves similarly to the 1-norm one. This indicates that the estimate for the 2-norm condition number (3.21) may not be optimal. Numerical analysis on the 2-norm condition number deserves further studies. Condition number properties for the matrix  $L - \frac{A^l}{2}$  in the semi-implicit trapezoidal scheme can be derived analogously.

**Remark 3.2.** Our numerical methods can be readily extended to three dimensions in a dimension-by-dimension manner. Numerical properties, such as positivity preserving and bounded condition number of the coefficient matrix, can be analogously proved.

#### 4. Numerical examples

In this section, we test numerical properties of the proposed numerical methods, and explore the steric effects on the ion distribution and conductance in a two-dimensional slit-shaped nanopore model, cf. the schematic view shown in Fig. 4.1. Although the proposed method allows a nonuniform mesh, we simply employ a uniform mesh with grid spacing  $h_m^x = h_m^y = h$  in the following simulations. Unless stated otherwise, we take the characteristic concentration  $c_0 = 1$  M, macroscopic characteristic length  $L = 1$  nm, and characteristic diffusion constant  $D_0 = 1$  nm<sup>2</sup>/ns.

##### 4.1. Accuracy and condition numbers

For simplicity, we consider an electrolyte solution with symmetric monovalent ions, and take  $\kappa = \frac{1}{6}$ , the steric interaction coefficient matrix

**Table 4.1**

The  $l^2$  error and convergence order for  $c^1$ ,  $c^2$ , and  $\phi$  by using the first-order semi-implicit scheme (3.12) with  $\Delta t = h^2$ .

$h$	$l^2$ error in $c^1$	Order	$l^2$ error in $c^2$	Order	$l^2$ error in $\phi$	Order
$\frac{1}{10}$	8.39e-002	-	8.39e-002	-	4.04e-002	-
$\frac{1}{15}$	3.88e-002	1.90	3.88e-002	1.90	2.27e-002	2.01
$\frac{1}{20}$	2.21e-002	1.95	2.21e-002	1.95	1.45e-002	2.00
$\frac{1}{25}$	1.43e-002	1.97	1.43e-002	1.97	1.01e-002	2.00

**Table 4.2**

The  $l^2$  error and convergence order for  $c^1$ ,  $c^2$ , and  $\phi$  by using the trapezoidal scheme (3.13) with  $\Delta t = h/10$ .

$h$	$l^2$ error in $c^1$	Order	$l^2$ error in $c^2$	Order	$l^2$ error in $\phi$	Order
$\frac{1}{10}$	9.04e-002	-	9.04e-002	-	9.12e-002	-
$\frac{1}{15}$	4.03e-002	1.99	4.03e-002	1.99	4.04e-002	2.01
$\frac{1}{20}$	2.23e-002	2.06	2.23e-002	2.06	2.27e-002	2.00
$\frac{1}{25}$	1.39e-002	2.10	1.39e-002	2.10	1.45e-002	2.00

$$W = \begin{pmatrix} 2 & 1 \\ 1 & 2 \end{pmatrix},$$

and  $\gamma^1 = \gamma^2 = 0.3$ , which correspond to diffusion constants  $D^1 = D^2 = 1 \text{ nm}^2/\text{ns}$ . To get a reference solution for comparison, we construct the following exact solution

$$\begin{cases} c^1 = 0.1e^{-t} \cos(\pi y) \sin\left(\frac{\pi x}{30}\right) + 0.2, \\ c^2 = 0.1e^{-t} \cos(\pi y) \sin\left(\frac{\pi x}{30}\right) + 0.2, \\ \psi = 5e^{-t} \cos(\pi y) \sin\left(\frac{\pi x}{60}\right), \end{cases} \quad (4.1)$$

to the problem

$$\begin{cases} \partial_t c^1 = \gamma^1 \nabla \cdot (\nabla c^1 + c^1 \nabla \phi + 2c^1 \nabla c^1 + c^1 \nabla c^2) + f_1, \\ \partial_t c^2 = \gamma^2 \nabla \cdot (\nabla c^2 - c^2 \nabla \phi + c^2 \nabla c^1 + 2c^2 \nabla c^2) + f_2, \\ -\kappa \Delta \phi = c^1 - c^2 + \rho^f. \end{cases}$$

The source terms  $f_1$ ,  $f_2$ , and  $\rho^f$ , and the initial and time-dependent boundary conditions are obtained with the known exact solution.

With the exact solution (4.1), we first test the spatial accuracy of the semi-implicit backward Euler scheme (3.12) by using various spatial step size  $h$  with a mesh ratio  $\Delta t = h^2$ . Note that such a mesh ratio is chosen for the purpose of numerical accuracy test, rather for the purpose of the stability or positivity. Table 4.1 lists  $l^2$  errors and convergence orders for ion concentrations and the electrostatic potential at time  $T = 0.2$ . The errors are obtained by comparing numerical solutions with the exact solution (4.1). We observe that the error decreases as the mesh refines, and that the convergence orders for ion concentrations and the potential are both about 2. This indicates that the semi-implicit scheme (3.12), as expected, is first-order and second-order accurate in time and spatial discretization, respectively.

We now test numerical accuracy of the semi-implicit trapezoidal scheme (3.13) with a time step size  $\Delta t = h/10$ . From Table 4.2, we can see that the numerical error decreases with a convergence order about 2, indicating that the trapezoidal scheme (3.13) has second-order accuracy in both time and spatial discretization.

It is well known that the accuracy, stability, and computational efficiency of the semi-implicit scheme are highly related to the condition number of the coefficient matrix  $B^l$  in (3.17). Theorem 3.2 establishes an upper bound estimate on the condition number of the matrix  $B^l$ . The upper bound indicates that the 1-norm condition number increases linearly with respect to  $\lambda^l := \gamma^l \Delta t / h^2$ . To further explore the dependence of condition number on mesh sizes, we perform numerical tests on both the 1-norm condition numbers  $\kappa_1(B^l)$  and 2-norm condition number  $\kappa_2(B^l)$  with various grid sizes. We take the following initial and boundary conditions

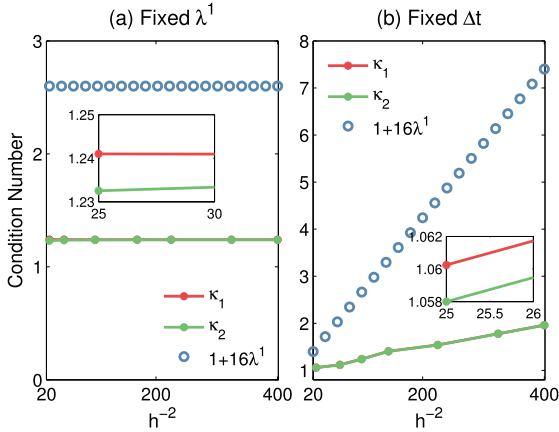


**Fig. 4.2.** The 1-norm and 2-norm condition numbers of the matrix  $B^1$ . (a) Fixed  $\lambda^1 := \gamma^1 \frac{\Delta t}{h^2}$ ; (b) Fixed  $\Delta t$ .

$$\left\{ \begin{array}{l} \phi(t, 0, y) = 5, \quad \phi(t, 30, y) = 0, \quad y \in [0, 1], \\ \frac{\partial \phi}{\partial y}(t, x, 0) = 5 \sin\left(\frac{\pi x}{5}\right), \quad \frac{\partial \phi}{\partial y}(t, x, 1) = -5 \sin\left(\frac{\pi x}{5}\right), \quad x \in [10, 20], \\ \frac{\partial \phi}{\partial y}(t, x, 0) = \frac{\partial \phi}{\partial y}(t, x, 1) = 0, \quad x \in [0, 10] \cup [20, 30], \\ c^1(0, x, y) = 0.1, \quad c^2(0, x, y) = 0.1, \quad (x, y) \in [0, 30] \times [0, 1], \\ c^1(t, 0, y) = 0.1, \quad c^1(t, 30, y) = 0.1, \quad c^2(t, 0, y) = 0.1, \quad c^2(t, 30, y) = 0.1, \quad y \in [0, 1], \\ \frac{\partial c^l}{\partial \mathbf{n}} + z^l c^l \frac{\partial \phi}{\partial \mathbf{n}} + c^l \sum_{r=1}^M w_{lr} \frac{\partial c^r}{\partial \mathbf{n}} = 0 \quad \text{on } \Gamma_N. \end{array} \right. \quad (4.2)$$

In the left plot of Fig. 4.2, with a fixed  $\lambda^1$ , we observe that  $\kappa_1(B^1)$  is almost constant with respect to  $h$ , implying that the condition number is a function of  $\lambda^1$ , as predicted by the upper bound given in Theorem 3.2. The right plot of Fig. 4.2 displays the condition numbers with a fixed value of  $\Delta t$ . One can observe that both the  $\kappa_1(B^1)$  and  $\kappa_2(B^1)$  are less than the predicted upper bound  $1 + 16\lambda^1$ , and both of them increase almost linearly with respect to  $h^{-2}$ . This again confirms that the condition number is a function of  $\lambda^1$ , as revealed by the Theorem 3.2.

It is interesting to point out that, in this simulation,  $\kappa_2(B^1)$  is almost the same as  $\kappa_1(B^1)$ . Although the estimate on  $\kappa_2(B^1)$  predicted by Theorem 3.2 is not optimal, our numerical results evidence that  $\kappa_2(B^1)$  behaves similarly to the  $\kappa_1(B^1)$ , in terms of the dependence on mesh sizes. Furthermore, numerical tests show that both the  $\kappa_1(B^1)$  and  $\kappa_2(B^1)$  are fairly small, indicating that our novel numerical schemes based on harmonic-mean approximations are stable and efficient.

#### 4.2. Steric interactions

##### 4.2.1. Self interactions

To study the effect of self steric interactions on the ion distribution, we use the following steric interaction coefficient matrices  $W$ :

$$\begin{pmatrix} 0 & 0 \\ 0 & 0 \end{pmatrix}, \quad \begin{pmatrix} 4 & 1 \\ 1 & 4 \end{pmatrix}, \quad \text{and} \quad \begin{pmatrix} 8 & 1 \\ 1 & 8 \end{pmatrix}.$$

We consider the steady-state SPNP equations with initial and boundary conditions given by (4.2).

As displayed in Fig. 4.3, ions accumulate at oppositely charged surfaces in all cases, due to electrostatic attraction. Without steric hindrance, large counterion concentration presents in the vicinity of charged surfaces, cf. the first plot of Fig. 4.3. With larger diagonal entries in  $W$ , both cations and anions have stronger self steric interactions, which lead to lower counterion concentration at the charged surface. This agrees with other modified PNP or PB models with steric effects [19, 20, 22, 43, 52]. Fig. 4.3 also illustrates that coions have slightly larger concentrations close to likely charged surfaces, when stronger steric interactions are incorporated. This demonstrates that the equilibrium distribution of ions is resulted from the competition between electrostatic interactions and steric interactions.

##### 4.2.2. Cross interactions

In order to understand cross steric interactions between different species of ions, we consider an electrolyte solution consists of two species of monovalent cations of different sizes and one species of monovalent anions. The off-diagonal

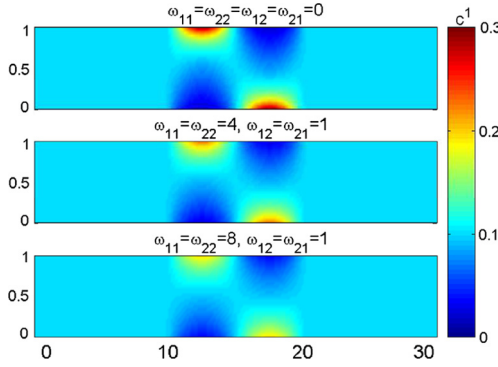


**Fig. 4.3.** Steady-state distribution of the concentration  $c^1$  with various  $W$ . (For interpretation of the colors in the figure(s), the reader is referred to the web version of this article.)

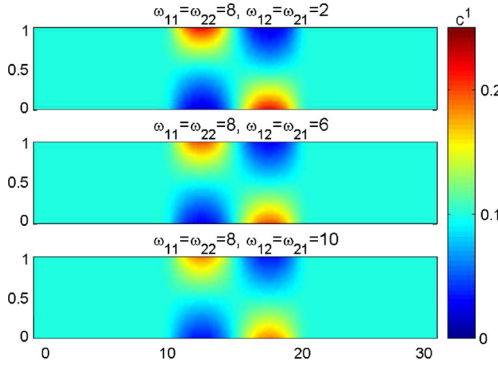


**Fig. 4.4.** Steady-state distribution of the concentration  $c^1$  with various off-diagonal entries  $\omega_{12}$  of  $W$ .

entries of the coefficient matrix  $W$ ,  $\omega_{12}$ , represents the cross steric interactions between the two species of cations. We conduct numerical simulations with the following steric interaction coefficient matrices  $W$ :

$$\begin{pmatrix} 8 & 2 & 1 \\ 2 & 8 & 1 \\ 1 & 1 & 4 \end{pmatrix}, \quad \begin{pmatrix} 8 & 6 & 1 \\ 6 & 8 & 1 \\ 1 & 1 & 4 \end{pmatrix}, \quad \text{and} \quad \begin{pmatrix} 8 & 10 & 1 \\ 10 & 8 & 1 \\ 1 & 1 & 4 \end{pmatrix}.$$

Notice that we here only vary  $\omega_{12}$  to focus on the impact of cross steric interactions between the cations. Also, we remark that the last matrix with strong cross steric interactions is indefinite. The initial and boundary conditions of ion concentrations are given by

$$\begin{cases} c^1(0, \cdot) = 0.1, \quad c^2(0, \cdot) = 0.1, \quad c^3(0, \cdot) = 0.2 & \text{in } \Omega, \\ c^1(t, \cdot) = c^2(t, \cdot) = 0.1, \quad c^3(t, \cdot) = 0.2 & \text{on } \Gamma_D, \\ \frac{\partial c^l}{\partial \mathbf{n}} + z^l c^l \frac{\partial \phi}{\partial \mathbf{n}} + c^l \sum_{r=1}^M w_{lr} \frac{\partial c^r}{\partial \mathbf{n}} = 0 & \text{on } \Gamma_N. \end{cases} \quad (4.3)$$

As shown in Fig. 4.4, the first species of cations are attracted to oppositely charged surfaces and repelled from the likely charged surfaces. With increasing  $\omega_{12}$ , the enhanced cross steric interactions strengthen the competition between cations, resulting in lower concentrations in the proximity of oppositely charged surfaces by steric repulsions. This indicates that the SPNP model is able to capture both the self steric interactions between the same species and cross steric interactions between different species in electric double layers. Our numerical simulations also demonstrate that the proposed numerical schemes work robustly for an indefinite matrix  $W$ , which may lead to multiple steady-state solutions to the SPNP equations [14,15].

#### 4.3. Current rectification

Ion current rectification has been observed in many nanopores and nanocapillaries [44]. Although concentrations of the electrolyte in contact are the same in two pore openings, asymmetric geometry and surface charge distribution can result

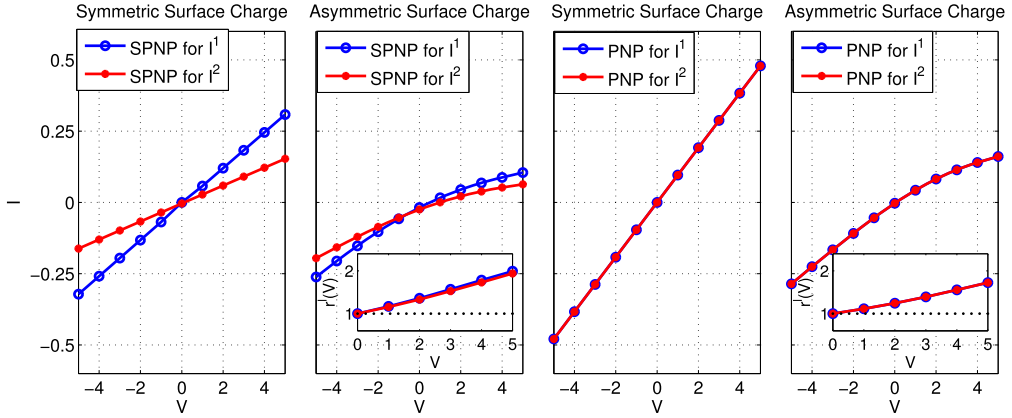


**Fig. 4.5.**  $I$ - $V$  curves of cations calculated by the steady-state SPNP and PNP equations with symmetric and asymmetric surface charges. The inset shows the rectification ratio against the applied potential differences.

in asymmetric current–voltage ( $I$ - $V$ ) curves [30,45]. Rectifying behavior due to asymmetric geometry has been numerically studied in conically shaped nanopores [47]. We now study ion conductance in a geometrically symmetric slit-shaped nanopore but with asymmetric surface charge distribution on walls of the nanopore:

$$\begin{cases} \frac{\partial\phi}{\partial y}(t, x, 0) = 5 \sin\left(\frac{\pi x}{5}\right), & x \in [10, 15], \quad \frac{\partial\phi}{\partial y}(t, x, 0) = 0, & x \in [0, 10] \cup [15, 30], \\ \frac{\partial\phi}{\partial y}(t, x, 1) = 5 \sin\left(\frac{\pi x}{5}\right), & x \in [15, 20], \quad \frac{\partial\phi}{\partial y}(t, x, 1) = 0, & x \in [0, 15] \cup [20, 30]. \end{cases}$$

For comparison, we refer the surface charge distribution given in (4.2) as the symmetric surface charge distribution. We again consider an electrolyte solution with two species of monovalent cations and one species of monovalent anions. The simulations use the steric interaction coefficient matrix

$$W = \begin{pmatrix} 4 & 1 & 1 \\ 1 & 8 & 1 \\ 1 & 1 & 2 \end{pmatrix},$$

which represents that the first species of cations have weaker self steric interactions than the second species of cations do. We calculate ion currents at the cross section in the middle by

$$I^l = - \int_0^1 D^l \left( \partial_x c^l + \beta q^l c^l \partial_x \psi + c^l \sum_{r=1}^M \omega_{lr} \partial_x c^r \right) \Big|_{x=15} dy \quad \text{for } l = 1, 2, 3.$$

Fig. 4.5 depicts the  $I$ - $V$  curves of the first and second species of cations with symmetric and asymmetric surface charges. For comparison, the results calculated by the PNP equations are shown as well. Since the classical PNP theory fails to capture the ion-specificity other than valence, the current profile of the first and second species of ions are indistinguishable. With the same voltage differences, the current  $I^2$  calculated by the SPNP equations is less than that of  $I^1$  and the currents predicted by the classical PNP theory, due to stronger self steric interactions. This agrees with the conclusion obtained by other steric modified PNP models that steric effects decrease ion conductance [41]. Obviously, the  $I$ - $V$  curves of the nanopore with symmetric surface charges are perfectly symmetric about the origin, showing no rectifying behavior for either the SPNP or PNP equations. In contrast, the  $I$ - $V$  curves of the nanopore with asymmetric surface charges present significant rectification phenomenon, i.e., the rectification ratio

$$r^l(V) := \left| \frac{I^l(-V)}{I^l(V)} \right| \neq 1,$$

as shown in the inset of Fig. 4.5. Of interest is that the rectification effect becomes slightly less pronounced when stronger self steric interactions come into play. This can be explained by the observation made above that steric interactions offset to some extent the electrostatic interactions between the ions and asymmetrically charged walls, which cause the rectification phenomenon [12].

## 5. Conclusions

In this work, we propose numerical methods for a PNP model with steric effects (SPNP), which is derived from a modified free-energy functional that incorporates the steric interaction energy. Central differencing schemes based on harmonic-mean approximations are proposed on a nonuniform mesh for the spatial discretization of the SPNP equations. Numerical analysis proves that the semi-implicit backward Euler discretization in time gives rise to a fully discrete scheme that can preserve solution positivity unconditionally, while the explicit forward Euler or semi-implicit trapezoidal discretization in time leads to a fully discrete scheme that ensures positivity under a constraint on a mesh ratio. Furthermore, an upper bound on condition numbers of the semi-implicit backward Euler discretization matrix of the modified Nernst–Planck equations is established. Numerical experiments are conducted to confirm the numerical analysis results including accuracy, bounded condition numbers, positivity, etc. We also apply the proposed schemes to study ion distribution and conductance of a slit-shaped nanopore with surface charges. We systematically evaluate the impact of self and cross steric interactions of ions on the ion distribution and rectifying behavior, further showing the effectiveness of the proposed schemes in solving problems of practical interest.

We now discuss several issues and possible further refinements of our work. The current development of numerical methods considers an open system partitioned with a nonuniform mesh in a regular domain. It is of practical interest to design numerical methods for irregular computational domains with various types of boundary conditions. The discretization accuracy on boundary grid points and numerical properties, such as positivity preservation and mass conservation at discrete level, are desirable to achieve. Such numerical properties are essential to the validity of numerical solutions to the PNP-type models. In addition, our second-order temporal discretization scheme preserves positivity under a constraint on the time stepsize. It is desirable to design an unconditionally positivity-preserving scheme while keeping the second-order accuracy.

The developed numerical methods can be readily extended to solve other modified PNP models. In general, the chemical potential can be considered in the form of  $\mu^l = \mu_{\text{dilute}}^l + \mu_{\text{excess}}^l$ , where the chemical potential for dilute solutions is often given by [1,19]

$$\mu_{\text{dilute}}^l = q^l \psi + \beta^{-1} \ln(\Lambda^3 c^l),$$

and the excess chemical potential  $\mu_{\text{excess}}^l$  is introduced to consider various effects that are neglected by the classical PB/PNP models. For instance, the excess chemical potential can express the electrostatic correlation based on mean spherical approximations [46], the Coulomb correlation in media of variable dielectric coefficient [29], and size effect either by hard-sphere repulsion described by the fundamental measure theory [42,48] or by the incorporation of the entropy of solvent molecules [3,19–21]. For such modified PNP models, the corresponding numerical methods can be analogously proposed based on (3.5) with

$$S^l = \beta q^l \psi + \beta \mu_{\text{excess}}^l.$$

The results on positivity and bounded condition numbers of the discretization matrix still hold for such extended numerical methods. It remains for future work to study those extended models on their numerical properties, such as free-energy dissipation, mass conservation, and numerical stability.

## Acknowledgements

J. Ding was supported by National Natural Science Foundation of China (No. 11601361, 21773165, 11771318, and 11790274). S. Zhou was supported by Natural Science Foundation of Jiangsu Province (BK20160302), National Natural Science Foundation of China (No. 11601361 and 21773165), and Soochow University through the grant (Q410700415). The authors thank Dr. Cheng Wang, Shixin Xu, and Xingye Yue for helpful discussions.

## References

- [1] M.Z. Bazant, M.S. Kilic, B.D. Storey, A. Ajdari, Towards an understanding of induced-charge electrokinetics at large applied voltages in concentrated solutions, *Adv. Colloid Interface Sci.* 152 (2009) 48–88.
- [2] M.Z. Bazant, K. Thornton, A. Ajdari, Diffuse-charge dynamics in electrochemical systems, *Phys. Rev. E* 70 (2004) 021506.
- [3] I. Borukhov, D. Andelman, H. Orland, Steric effects in electrolytes: a modified Poisson–Boltzmann equation, *Phys. Rev. Lett.* 79 (1997) 435–438.
- [4] J.H. Chaudhry, J. Comer, A. Aksimentiev, L. Olson, A stabilized finite element method for modified Poisson–Nernst–Planck equations to determine ion flow through a nanopore, *Commun. Comput. Phys.* 15 (2014) 93–125.
- [5] J. Ding, H. Sun, Z. Wang, S. Zhou, Computational study on hysteresis of ion channels: multiple solutions to steady-state Poisson–Nernst–Planck equations, *Commun. Comput. Phys.* 23 (5) (2018) 1549–1572.
- [6] J. Ding, C. Wang, S. Zhou, Optimal rate convergence analysis of a second order numerical scheme for the Poisson–Nernst–Planck system, *Numer. Math., Theory Methods Appl.* 12 (2019) 607–626, <https://doi.org/10.4208/nmtma.OA-2018-0058>.
- [7] W. Fang, K. Ito, Asymptotic behavior of the drift-diffusion semiconductor equations, *J. Differ. Equ.* 123 (1995) 567–587.
- [8] W. Fang, K. Ito, Global solutions of the time-dependent drift-diffusion semiconductor equations, *J. Differ. Equ.* 123 (1995) 523–566.
- [9] A. Flavell, J. Kabre, X. Li, An energy-preserving discretization for the Poisson–Nernst–Planck equations, *J. Comput. Electron.* 16 (2017) 431–441.
- [10] A. Flavell, M.M. Machen, R. Eisenberg, J. Kabre, C. Liu, X. Li, A conservative finite difference scheme for Poisson–Nernst–Planck equations, *J. Comput. Electron.* 13 (2014) 235–249.

- [11] H. Gajewski, K. Gröger, On the basic equations for carrier transport in semiconductors, *J. Math. Anal. Appl.* 113 (1986) 12–35.
- [12] T. Gamble, K. Decker, T.S. Plett, M. Pevarnik, J. Pietschmann, I. Vlassiouk, A. Aksimentiev, Z.S. Siwy, Rectification of ion current in nanopores depends on the type of monovalent cations: experiments and modeling, *J. Phys. Chem. B* 118 (18) (2014) 9809–9819.
- [13] H. Gao, D. He, Linearized conservative finite element methods for the Nernst-Planck-Poisson equations, *J. Sci. Comput.* 72 (2017) 1269–1289.
- [14] N. Gavish, Poisson-Nernst-Planck equations with steric effects-non-convexity and multiple stationary solutions, *Physica D* 368 (2018) 50–65.
- [15] N. Gavish, C. Liu, B. Eisenberg, Do bistable steric Poisson-Nernst-Planck models describe single-channel gating?, *J. Phys. Chem. B* 22 (20) (2018) 5183–5192.
- [16] G. Golub, C. Loan, *Matrix Computations*, Johns Hopkins Studies in the Mathematical Sciences, Johns Hopkins University Press, 1996.
- [17] T. Horng, T. Lin, C. Liu, B. Eisenberg, PNP equations with steric effects: a model of ion flow through channels, *J. Phys. Chem. B* 116 (2012) 11422–11441.
- [18] Y. Hyon, B. Eisenberg, C. Liu, A mathematical model for the hard sphere repulsion in ionic solutions, *Commun. Math. Sci.* 9 (2010) 459–475.
- [19] M.S. Kilic, M.Z. Bazant, A. Ajdari, Steric effects in the dynamics of electrolytes at large applied voltages. I. Double-layer charging, *Phys. Rev. E* 75 (2007) 021502.
- [20] M.S. Kilic, M.Z. Bazant, A. Ajdari, Steric effects in the dynamics of electrolytes at large applied voltages. II. Modified Poisson-Nernst-Planck equations, *Phys. Rev. E* 75 (2007) 021503.
- [21] B. Li, Continuum electrostatics for ionic solutions with nonuniform ionic sizes, *Nonlinearity* 22 (2009) 811–833.
- [22] B. Li, P. Liu, Z. Xu, S. Zhou, Ionic size effects: generalized Boltzmann distributions, counterion stratification, and modified Debye length, *Nonlinearity* 26 (10) (2013) 2899.
- [23] T. Lin, B. Eisenberg, A new approach to the Lennard-Jones potential and a new model: PNP-steric equations, *Commun. Math. Sci.* 12 (2014) 149–173.
- [24] T. Lin, B. Eisenberg, Multiple solutions of steady-state Poisson-Nernst-Planck equations with steric effects, *Nonlinearity* 28 (2015) 2053–2080.
- [25] H. Liu, Z. Wang, A free energy satisfying finite difference method for Poisson-Nernst-Planck equations, *J. Comput. Phys.* 268 (2014) 363–376.
- [26] H. Liu, Z. Wang, A free energy satisfying discontinuous Galerkin method for one-dimensional Poisson-Nernst-Planck systems, *J. Comput. Phys.* 328 (2017) 413–437.
- [27] H. Liu, H. Yu, Maximum-principle-satisfying third order discontinuous Galerkin schemes for Fokker-Planck equations, *SIAM J. Sci. Comput.* 36 (5) (2014) A2296–A2325.
- [28] H. Liu, H. Yu, The entropy satisfying discontinuous Galerkin method for Fokker-Planck equations, *J. Sci. Comput.* 62 (2015) 803–830.
- [29] P. Liu, X. Ji, Z. Xu, Modified Poisson-Nernst-Planck model with accurate Coulomb correlation in variable media, *SIAM J. Appl. Math.* 78 (2018) 226–245.
- [30] X. Liu, B. Lu, Incorporating born solvation energy into the three-dimensional Poisson-Nernst-Planck model to study ion selectivity in KcsA  $K^+$  channels, *Phys. Rev. E* 96 (2017) 062416.
- [31] X. Liu, Y. Qiao, B. Lu, Analysis of the mean field free energy functional of electrolyte solution with non-homogenous boundary conditions and the generalized PB/PNP equations with inhomogeneous dielectric permittivity, *SIAM J. Appl. Math.* 78 (2) (2018) 1131–1154.
- [32] B. Lu, M.J. Holst, J.A. McCammon, Y. Zhou, Poisson-Nernst-Planck equations for simulating biomolecular diffusion-reaction processes I: finite element solutions, *J. Comput. Phys.* 229 (19) (2010) 6979–6994.
- [33] B. Lu, Y. Zhou, Poisson-Nernst-Planck equations for simulating biomolecular diffusion-reaction processes II: size effects on ionic distributions and diffusion-reaction rates, *Biophys. J.* 100 (2011) 2475–2485.
- [34] P. Markowich, *The Stationary Semiconductor Device Equations*, Springer-Verlag, New York, 1986.
- [35] D. Meng, B. Zheng, G. Lin, M. Sushko, Numerical solution of 3D Poisson-Nernst-Planck equations coupled with classical density functional theory for modeling ion and electron transport in confined environment, *Commun. Comput. Phys.* 16 (2014) 1298–1322.
- [36] M.S. Metti, J. Xu, C. Liu, Energetically stable discretizations for charge transport and electrokinetic models, *J. Comput. Phys.* 306 (2016) 1–18.
- [37] M. Mirzadeh, F. Gibou, A conservative discretization of the Poisson-Nernst-Planck equations on adaptive Cartesian grids, *J. Comput. Phys.* 274 (2014) 633–653.
- [38] M. Mock, An initial value problem from semiconductor device theory, *SIAM J. Math. Anal.* 5 (1974) 597–612.
- [39] A. Prohl, M. Schmuck, Convergent discretizations for the Nernst-Planck-Poisson system, *Numer. Math.* 111 (2009) 591–630.
- [40] Y. Qiao, X. Liu, M. Chen, B. Lu, A local approximation of fundamental measure theory incorporated into three dimensional Poisson-Nernst-Planck equations to account for hard sphere repulsion among ions, *J. Stat. Phys.* 163 (2016) 156–174.
- [41] Y. Qiao, B. Tu, B. Lu, Ionic size effects to molecular solvation energy and to ion current across a channel resulted from the nonuniform size-modified PNP equations, *J. Chem. Phys.* 140 (2014) 174102.
- [42] R. Roth, R. Evans, A. Lang, G. Kahl, Fundamental measure theory for hard-sphere mixtures revisited: the white bear version, *J. Phys. Condens. Matter* 14 (46) (2002) 12063.
- [43] F. Siddiqua, Z. Wang, S. Zhou, A modified Poisson-Nernst-Planck model with excluded volume effect: theory and numerical implementation, *Commun. Math. Sci.* 16 (1) (2018) 251–271.
- [44] Z. Siwy, Ion-current rectification in nanopores and nanotubes with broken symmetry, *Adv. Funct. Mater.* 16 (2006) 735–746.
- [45] Z. Siwy, E. Heins, C.C. Harrell, P. Kohli, C.R. Martin, Conical-nanotube ion-current rectifiers: the role of surface charge, *J. Am. Chem. Soc.* 126 (2004) 10850–10851.
- [46] E. Waisman, J.L. Lebowitz, Mean spherical model integral equation for charged hard spheres II. results, *J. Chem. Phys.* 57 (1972) 3093–3099.
- [47] J. Xu, B. Lu, L. Zhang, A time-dependent finite element algorithm for simulations of ion current rectification and hysteresis properties of 3D nanopore system, *IEEE Trans. Nanotechnol.* 17 (2018) 513–519.
- [48] Y. Yu, J. Wu, Structures of hard-sphere fluids from a modified fundamental measure theory, *J. Chem. Phys.* 117 (22) (2002) 10156–10164.
- [49] J. Zheng, M. Trudeau, *Handbook of Ion Channels*, CRC Press, 2015.
- [50] Q. Zheng, D. Chen, G.W. Wei, Second-order Poisson-Nernst-Planck solver for ion channel transport, *J. Comput. Phys.* 230 (13) (2011) 5239–5262.
- [51] J. Zhou, Y. Jiang, M. Doi, Cross interaction drives stratification in drying film of binary colloidal mixtures, *Phys. Rev. Lett.* 10 (2017) 108002.
- [52] S. Zhou, Z. Wang, B. Li, Mean-field description of ionic size effects with non-uniform ionic sizes: a numerical approach, *Phys. Rev. E* 84 (2011) 021901.